CONFERENCE PRE-PRINT

CORRECTION OF 1/1 AND 2/2 ERROR FIELD IN WENDELSTEIN 7-X VIA DIVERTOR HEAT LOAD SYMMETRIZATION

[1]Y. GAO, S. BOZHENKOV, Y. FENG, S. THIEDE, M. JAKUBOWSKI, J. GEIGER, T. STANGE, O. GRULKE, M. ENDLER, M. OTTE, D. NAUJOKS, J. FELLINGER, [2]F. PISANO AND THE W7-X TEAM[a]

[1]Max-Planck-Institut für Plasmaphysik, Germany
[2]University of Cagliari, Italy
[a]See Grulke et al 2024 (https://doi.org/10.1088/1741-4326/ad2f4d) for the W7-X Team.

Email: yu.gao@ipp.mpg.de

Abstract

Recent experiments with the water-cooled, high-heat-flux divertor of the Wendelstein 7-X (W7-X) stellarator demonstrate substantial progress in error field correction. Numerical simulations reveal a pronounced sensitivity of divertor heat load distributions to error fields. Experimentally, wide-angle infrared cameras monitoring all ten divertor units show significant improvements in the symmetry of divertor thermal footprints when trim coils and control coils are employed to compensate intrinsic 1/1 and 2/2 error fields, respectively. The experimentally determined amplitude of the intrinsic 1/1 error field is consistent with results obtained seven years ago, despite different diagnostics, divertor components, and analysis techniques. For the first time, the intrinsic 2/2 error field has been corrected through a phase-scan experiment using control coil currents, supported and validated by simulations.

1. INTRODUCTION

One of the central challenges for future fusion reactors is the management of power exhaust. Wendelstein 7-X (W7-X), the world's most advanced stellarator, is the first device to employ an actively cooled island divertor and is among the few long-pulse magnetic confinement devices capable of sustaining high heat fluxes. The intrinsic three-dimensional (3D) magnetic island structure at the plasma boundary in W7-X produces non-axisymmetric heat deposition across the ten divertor units. Although the magnetic coil system provides substantial flexibility in shaping the edge magnetic topology [1], further modifications to the thermal footprint arise from finite error fields [2,3], toroidal plasma currents, plasma beta effects, and particle drifts. Heat transport has also been observed in geometrically shadowed divertor regions.

For safe operation, real-time monitoring of all ten divertor units is essential. This is achieved using infrared thermographic systems [4,5] equipped with wide-angle optics. The temperature evolution measured on the divertor target surface is processed with the newly developed DELVER code (Divertor Energy Load Versatile EstimatoR) [6], a 3D implicit anisotropic heat diffusion solver capable of handling heat transport across multiple material layers, including the carbon-fiber composite, interlayers, and heat sink. DELVER also incorporates water-cooling conditions at the base and includes at the top surface layer [7] adjustments.

In this study, divertor heat flux distributions across all units are utilized for error field correction. For the first time, control coils are employed to mitigate intrinsic 2/2 error fields using a carefully designed phase-scan experiment. The results demonstrate clear improvements in symmetry, comparable to those achieved in 1/1 error field correction with trim coils. This paper presents both the preparatory simulations for coil current waveforms and the results of phase-scan experiments.

2. ERROR FIELD CORRECTION

W7-X is designed with a five-fold toroidal modular and an up-down flip symmetry. The ten divertor units are arranged toroidally, with five in the upper half and five in the lower half of the machine (Fig. 1). Ideally, heat loads would be equally distributed among the ten units; however, asymmetries arise due to error fields and particle drifts. Particle drifts primarily cause global up-down asymmetries, which are beyond the scope of this work. Error fields originate from finite imperfections in coil manufacturing, installation misalignments, electromagnetic deformations, and ferromagnetic materials. In the standard magnetic configuration of W7-X, the boundary rotational transform is close to unity. The boundary 5/5 island chain (n/m = 5/5, m, n for poloidal and toroidal mode number, respectively) is strongly affected by low-order resonant 1/1 and 2/2 error fields, while higher-order modes exert less influence on flux surface displacement and island width [2]. These error fields destroy symmetry, producing uneven power deposition across the ten divertor units and increase the risk of localized overloading of plasma-facing components.

Five external trim coils [8] are designed to compensate intrinsic 1/1 error fields. Additionally, ten control coils [9], typically used to modify boundary island structure, can be employed to correct 2/2 error fields. Previous studies [2,3] demonstrated effective mitigation of the 1/1 error field by adjusting the amplitude and phase of trim coil currents. This was verified through flux surface mapping [10] and thermocouple measurements on the test divertor units. Predictions for the amplitude and phase of the 2/2 error field, following successful 1/1 correction, were derived by fitting flux surface mapping data [2].

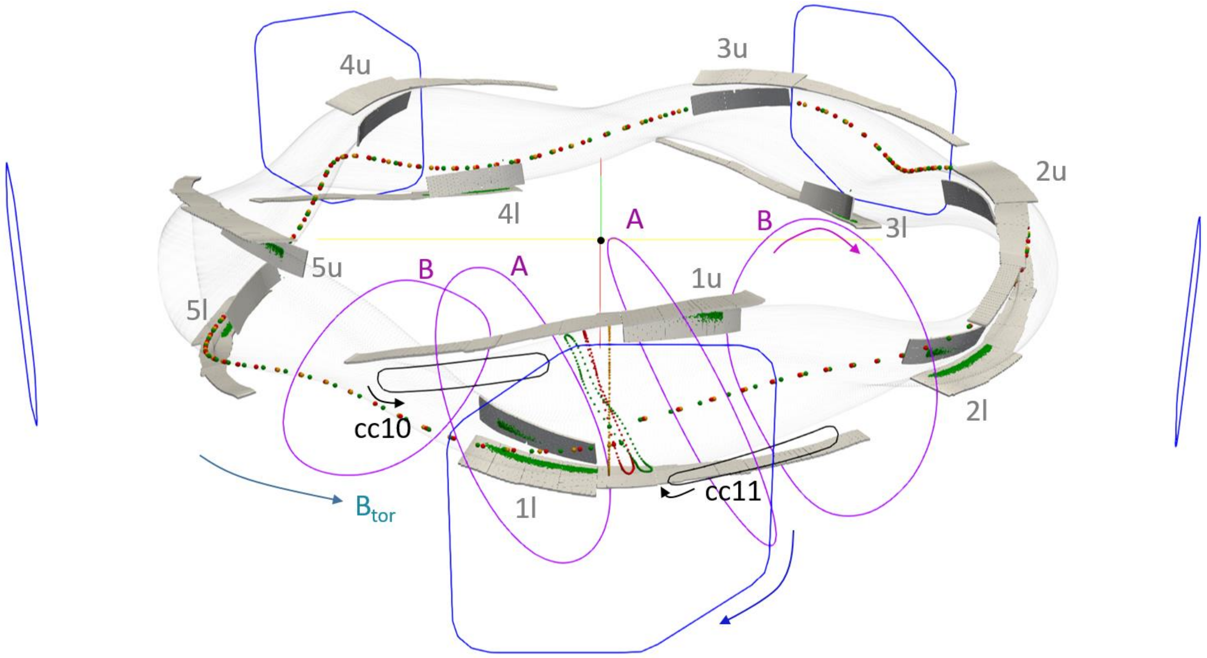

FIG. 1 Overview of the ten divertor units and the coil system in W7-X. Each divertor unit comprises one horizontal and one vertical target and is labeled 1–5 for the upper (u) and lower (l) halves of the device. Four planar coils of types A and B in module 1 are shown in purple, and two control coils (cc10 and cc11) in the same module are shown in black. These coils respect the five-fold machine symmetry, though only those in module 1 are displayed for clarity. The five trim coils are indicated in blue. Positive current directions are denoted by colored arrows. The geometric toroidal angle $\varphi_g = 0^\circ$ *is defined at the center of module 1, with the positive toroidal field directed counter-clockwise when viewed from above. The* $\varphi = 0^\circ$ *plane and representative field lines in Boozer, Hamada, and PEST flux coordinates are plotted in red, green, and orange, respectively. The global Cartesian origin of W7-X is marked as a black dot at the figure center.*

2.1. Simulation preparation

2.1.1. Coil currents for error field correction.

Previous corrections of the 1/1 error field employed amplitude and phase scans of trim coil currents based on cosine waveforms [3]. In this work, control coils are introduced for the first time to correct 2/2 error fields. A central question is determining the appropriate current settings in the control coils to generate the desired perturbation fields. To study the perturbation fields with different mode numbers, one needs to work in Fourier space. There are mainly three steps for this study.

(1) Constructing flux coordinates for a flux surface in the vicinity inside the last closed flux surface (LCFS), and decomposing them into Fourier components [11]:

$$\{R, z\} = \sum_{mn}\{R_{mn}, z_{mn}\}e^{i(m\iota+sn)\varphi},\ \varphi_g = \varphi + \sum_{mn}\varphi_{mn}e^{i(m\iota+sn)\varphi}.$$

Here $s = 5$ is the W7-X modular symmetry. In Fig. 1, three flux coordinates are computed at the LCFS, where along a field line $\theta = \iota\varphi$ always holds. Their $\varphi = 0^\circ$ plane, together with a field line traced from the outer mid-plane for one full toroidal turn inside the vessel are compared. In the PEST coordinate system, φ coincides with the geometric toroidal angle φ_g of the W7-X global coordinate system.

(2) Calculating Fourier spectra for the perturbation fields produced by individual coils. The normalized normal mode of a perturbation field $\vec{B}_{pert}$ is defined as Fourier decomposition of the field component perpendicular to the flux surface in Boozer coordinate calculated in the first step [2]:

$$b_{mn} = \frac{1}{rR_0B_0} \cdot \left(\vec{B}_{pert} \cdot \left[\frac{\partial \vec{r}}{\partial \theta} \times \frac{\partial \vec{r}}{\partial \varphi}\right]\right)_{mn}.$$

As an example, Fig. 2 shows the Fourier spectra at the LCFS generated by a 21 A winding current in trim coil 1 (trim1, located on the outboard side of module 1 with 48 windings) and a 125 A winding current in control coil 10 (cc10, positioned at half-module 10 with 8 windings). Because each coil occupies a specific toroidal angle in real space, the resulting toroidal modes are broadly distributed in Fourier space. The dominant poloidal mode numbers are 1 for trim1 and 2, 3, 4 for cc10, respectively.

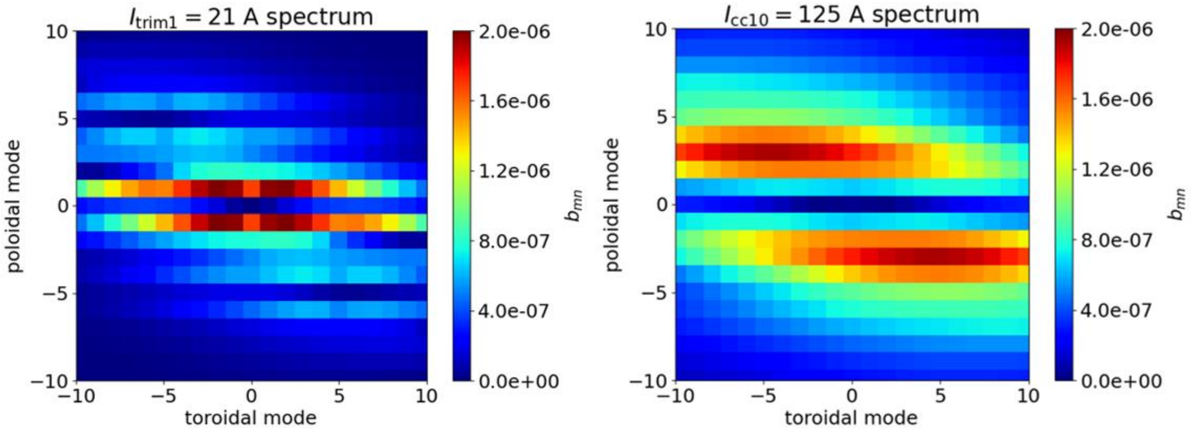

FIG. 2 Power spectra of individual coils at the LCFS. The left panel shows results for a 21 A winding current in trim coil 1, while the right panel corresponds to a 125 A winding current in control coil 10.

(3) Employing an optimization algorithm to determine current combinations that achieve target modes while suppressing unwanted harmonics. For the trim coils, for example, the target is set to $b_{11} = A \cdot e^{i\varphi_g}$, while other dominant modes at $\iota = 1$ are constrained to zero. With the spectra of individual coils with unit currents obtained in the second step, the optimization effectively determines the optimal coil currents approaching the target modes as weighted combinations, given the linear superposition of their Fourier spectra. Fig. 3 presents the optimization results, where a mode amplitude of $A = 0.5 \cdot 10^{-4}$ and phase $\varphi_g = 0^\circ$ are prescribed for both the b_{11} and b_{22} fields using the five trim coils and ten control coils, respectively. Note that the amplitude of b_{11} is the sum of the $(1, -1)$ mode and its complex conjugate $(-1, 1)$. While higher harmonics at $\iota = 1$ can be effectively suppressed, non-resonant sidebands (e.g. b_{14} in the trim coil case and b_{37} in the control coil case) remain unavoidable, though their influence on the boundary 5/5 island topology is expected to be minor. Furthermore, the optimized coil currents can be accurately fitted by a $cos\varphi$ wave for the trim coils and a $cos2\varphi$ wave for the control coils, with negligible fitting errors when plotted against the toroidal center of the relevant coils. For instance, the central positions of cc10 and cc11 are at −15° and +15°, respectively.

A unique relationship is found between the phase shift of the cosine waveform describing the coil currents and the phase of the resulting perturbation field. This correlation enables straightforward preparation of phase-scan experiments for error field correction by sampling different phases of the coil current waveform. In these experiments, the phase of the perturbation field (b_{11} and b_{22}) is used as the reference throughout the paper. A perturbation with phase of 0° has its maximal outward pointing field at the outboard side in the plane $\varphi_g = 0^\circ$ in W7-X global coordinate, as previously defined in [2].

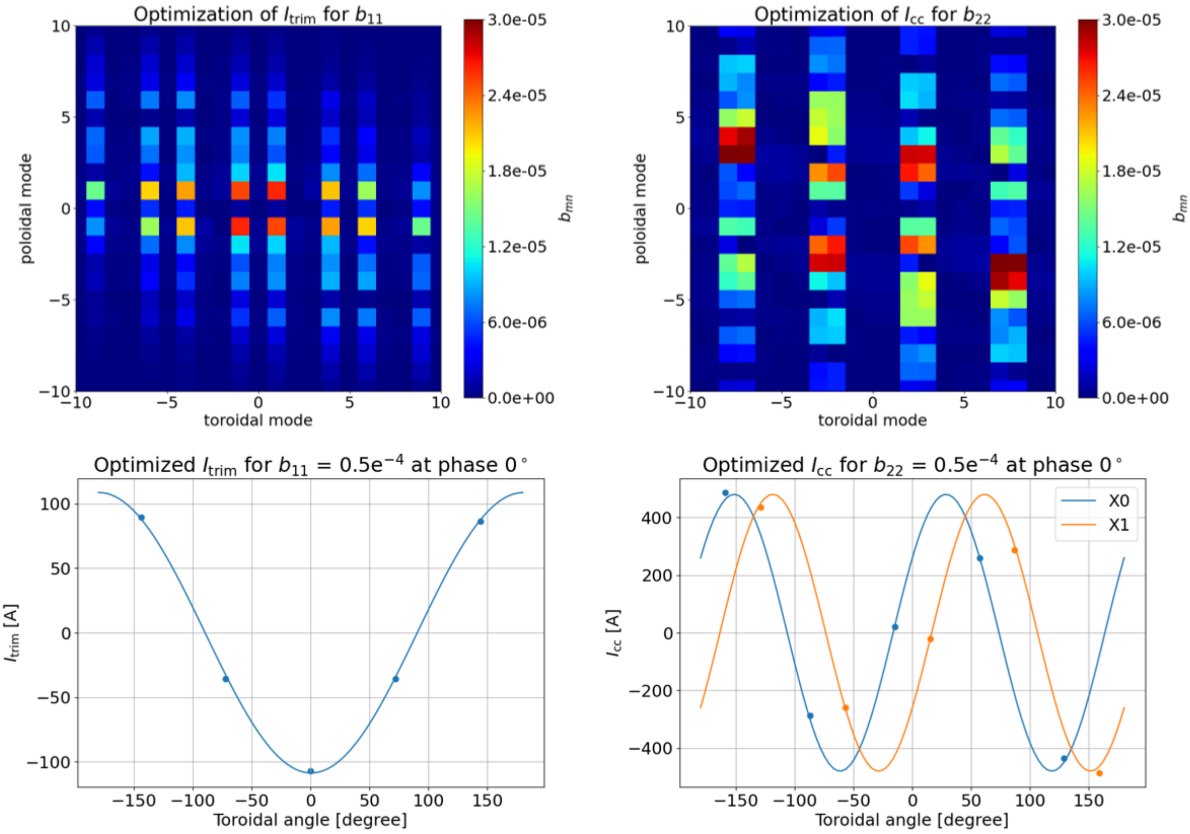

FIG. 3 Optimized coil currents (lower panels) and the corresponding Fourier spectra (upper panels). The left column shows results for b_{11}, and the right column for b_{22}. In the coil current plots, dots represent the values obtained from the optimization function, while the curves indicate fits using simple cosine waveforms.

2.1.2. Perturbation field effect on divertor heat loads

To quickly estimate heat load distributions in the presence of external perturbation fields, the EMC3-Lite code [12] is employed. This code simplifies the heat transport equation by considering only parallel electron heat conduction and perpendicular heat diffusion terms:

$$\nabla \cdot (-\kappa_e \nabla_{\parallel} T - \chi n \nabla_{\perp} T) = 0.$$

Here, it is assumed that the electron and ion temperatures are equal, i.e., $T = T_i = T_e$, and also for the density $n = n_i = n_e$ for the simulated hydrogen plasmas. The perpendicular heat diffusion coefficient is defined as $\chi = \chi_i + \chi_e$. At the target, the Bohm sheath boundary condition is applied within EMC3-Lite. In ideal simulations without external perturbation fields, the simulated target heat loads are identical across different target units.

Fig. 4 presents the simulation results of integrated heat loads corresponding to the fitted coil currents shown in Figure 3. Notably, the thermal loads on the targets can also be approximated using cosine functions, similar to the fitting performed for the coil currents ($a_0 + a_1 cos\varphi$ for 1/1 field, and $a_0 + a_2 cos2\varphi$ for 2/2 field). The upper and lower targets are fitted separately, and the toroidal angle at the center of each target unit is used for plotting. Interestingly, when both the trim and control coils are applied simultaneously, the heat load distribution appears to be approximately superimposed and can be described by a combined function, $a_0 + a_1 cos\varphi + a_2 cos2\varphi$. By comparing the fitted coefficients (shown in the figure legends) across all three cases, it is evident that the contributions from b_{11} and b_{22} can be partially disentangled from the integral target power. The fitting is not exact, particularly in the superimposed case, where overfitting is observed. This discrepancy may arise from sidebands, as illustrated in Fig. 3, which have minor effects on the edge topology.

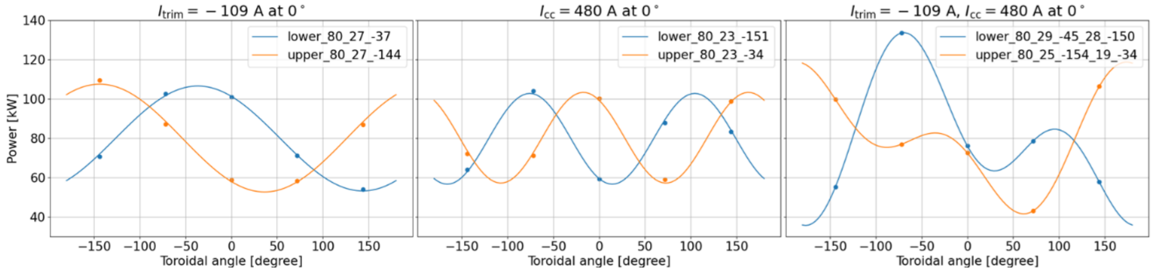

FIG. 4 Simulated integrated power on five upper (orange) and five lower (blue) divertor units under specific trim coil currents (left) and control coil currents (middle), as shown in Fig. 3, as well as for the case of superimposed trim and control coil currents (right). The corresponding fitting coefficients are indicated in the legends of each panel.

The simulation results were obtained using a total input power of 800 kW, a separatrix electron temperature $T_e = 100$ eV, a density $n_e = 1 \cdot 10^{19}\ \mathrm{m}^{-3}$, and a perpendicular heat diffusion coefficient $\chi = 1\ \mathrm{m}^2/\mathrm{s}$. Increasing χ reduces the asymmetry across different target units due to the smoothing effect of diffusion. Conversely, when asymmetry is enhanced, either by a stronger perturbation field (e.g., mode amplitude A > $1 \cdot 10^{-4}$) or by a significantly reduced $\chi < 0.1\ \mathrm{m}^2/\mathrm{s}$, the fitting procedure may fail, particularly if almost no power is deposited on certain divertor units.

2.2. Experimental results

A phase-scan experiment comprising a sequence of discharges was performed at the beginning of the recent campaign to identify optimal coil settings for error field correction. Experiments were conducted in the standard magnetic configuration without planar coil currents, with 1.8 MW of electron cyclotron resonance heating and line-integrated density of $2 \cdot 10^{19}\ \mathrm{m}^{-2}$. Specific perturbation phases were generated using trim and control coil currents (Table 1).

TABLE 1. Phase scan experiment performed on 20240918. Table includes program ID, amplitude of the coil current waveform, and the relevant phase of the produced b_{11} and b_{22} perturbation fields.

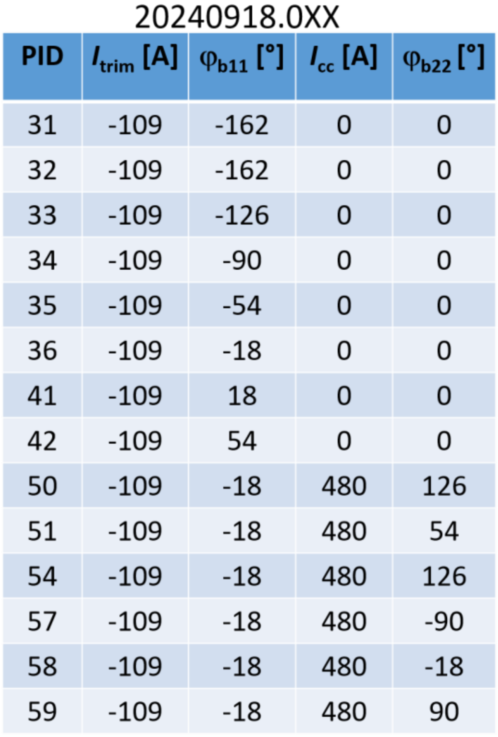

20240918.0XX

PID	I_{trim} [A]	φ_{b11} [°]	I_{cc} [A]	φ_{b22} [°]
31	-109	-162	0	0
32	-109	-162	0	0
33	-109	-126	0	0
34	-109	-90	0	0
35	-109	-54	0	0
36	-109	-18	0	0
41	-109	18	0	0
42	-109	54	0	0
50	-109	-18	480	126
51	-109	-18	480	54
54	-109	-18	480	126
57	-109	-18	480	-90
58	-109	-18	480	-18
59	-109	-18	480	90

The relative standard deviation (Rstd) of the integrated divertor power is calculated separately for the five upper and five lower targets. The mean of these two Rstd values is then used to quantify the symmetry level for a given phase:

$$\mu = \frac{1}{5}\sum_{t=1}^{5} P_t,\ R = \frac{\sigma}{\mu} = \frac{\sqrt{\sum_{t=1}^{5}(P_t-\mu)^2}}{5\mu},\ Rstd = \frac{1}{2}(R_{up} + R_{low}).$$

The amplitudes of the intrinsic b_{11} and b_{22} error fields are assumed to be approximately $0.5 \cdot 10^{-4}$, based on previous experimental results and simulation studies [2,3]; therefore, no amplitude scans are conducted in this campaign. To generate a b_{11} field of this magnitude at the LCFS, a trim coil current amplitude of 109 A is required. Similarly, producing a b_{22} field of comparable strength requires 480 A for the control coils. See Fig. 3 for further details.

Fig. 5 summarizes the results. A phase scan of b_{11} is performed first, showing that Rstd reaches a minimum near $\varphi_g = -18°$. And the closer the phase is to $-18°$, the better the heat load symmetry. This “valley-shaped” profile of Rstd as a function of phase provides confidence in the use of infrared cameras for error field correction. The results indicate the presence of an intrinsic b_{11} field with a specific orientation, corresponding to the phase opposite to that of the optimal correction field generated by the trim coils during the phase scans, i.e., at $\varphi_g = -18° + 180° = 162°$.

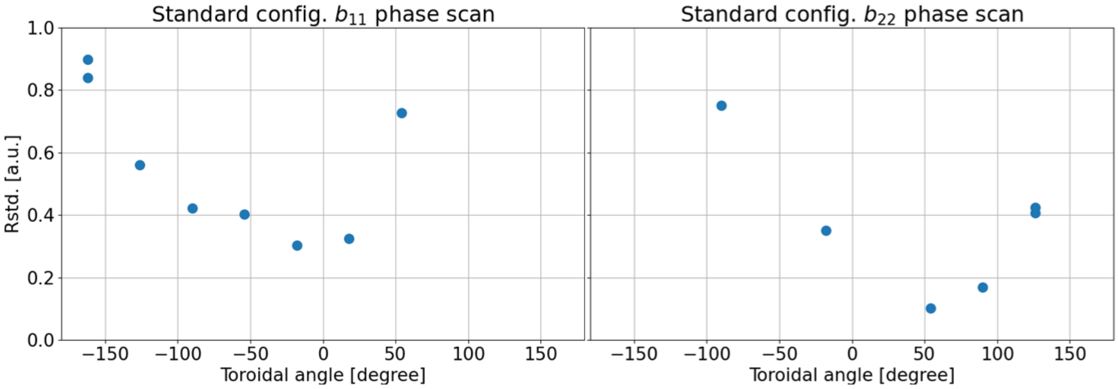

FIG. 5 Experimental results of the Rstd of the integrated power on all divertor units for different phases of the perturbation field. Left: Phase scan of the b_{11} field using trim coils. Right: Phase scan of the b_{22} field using control coils, with the optimal trim coil settings applied for b_{11} error field correction.

Building on the optimal trim coil settings, a phase scan of the control coils is performed to probe the phase of the remaining intrinsic b_{22} field. A “valley” in Rstd is again observed, with a minimum at $\varphi_g = 54°$, indicating that the intrinsic b_{22} field has a phase of $\varphi_g = 54° - 180° = -126°$. While the minimum Rstd obtained with b_{11} error field correction saturates at approximately 0.3, it can be further reduced to 0.1 with the additional b_{22} error field correction. This confirms that the intrinsic b_{11} and b_{22} error fields are of similar magnitude, approximately $0.5 \cdot 10^{-4}$, as both are effectively compensated by the combined action of the trim and control coils, producing b_{11} and b_{22} fields of the same strength.

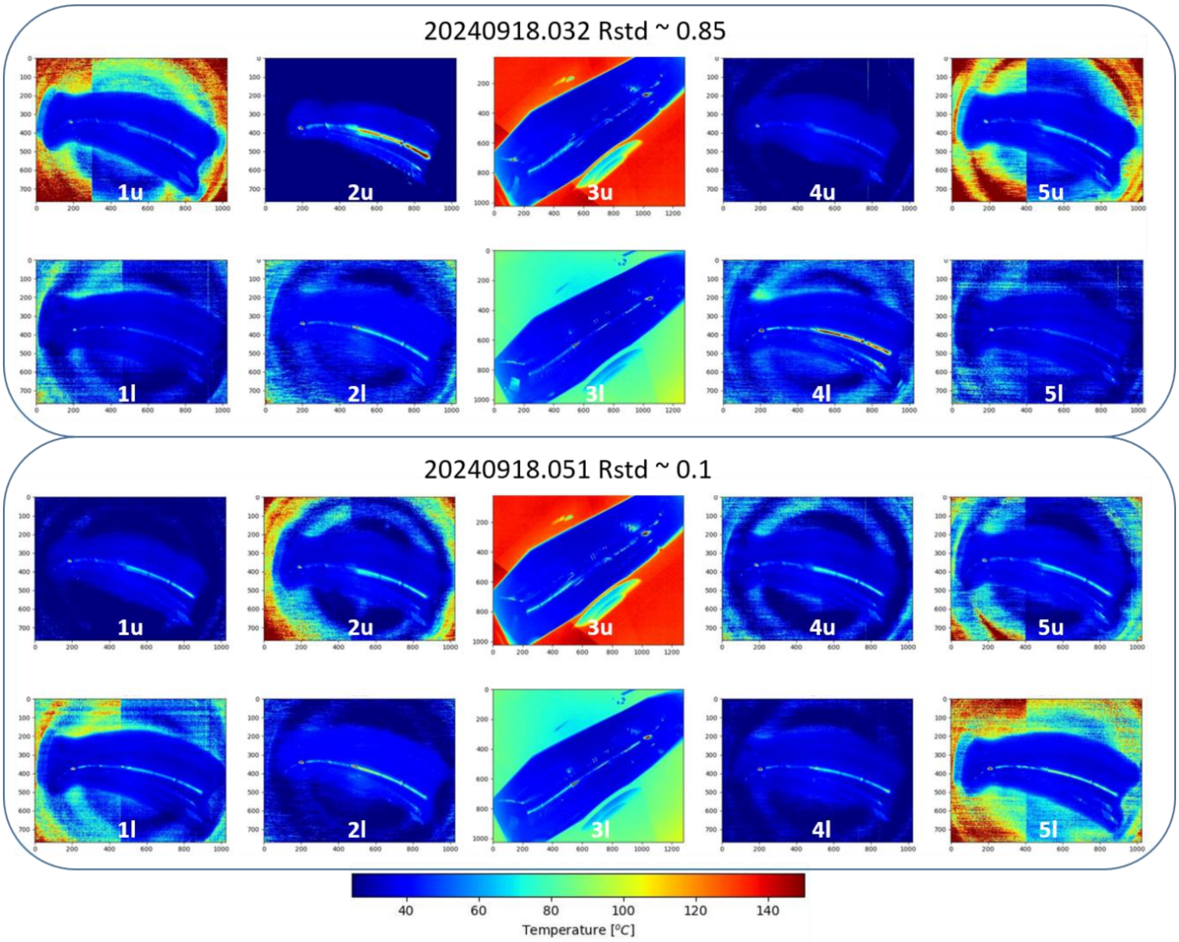

FIG. 6 Measured temperature distributions for the most asymmetric (upper) and symmetric (lower) case.

Fig. 6 compares the measured tempearture distributions for all 10 divertor units between the most asymmetric and symmetric case. In the case with the largest Rstd, most heat load is concentrated on specific divertor units (e.g., 2u and 4l), while units such as 1l, 4u, and 5l receive significantly less heat. With the optimal trim and control coil settings for error field correction, the heat loads are nearly uniform across all target units.

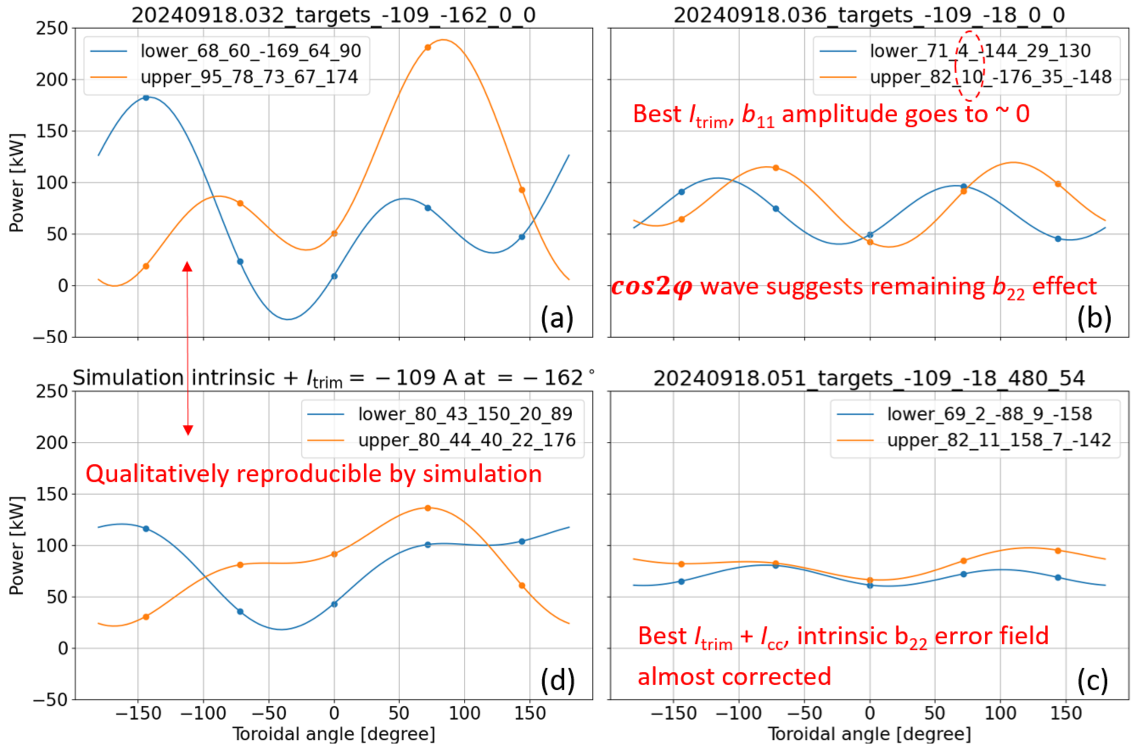

FIG. 7 Waveform of integral power on divertor units. (a) Experimental result from 20240918.032 with $I_{trim} = -109$ A at $\varphi = -162^{\circ}$. (b) Result with the optimal trim coil setting in 20240918.036. (c) Result with *both optimal trim and control coil settings in 20240918.051. (d) Simulated result with derived intrinsic error field plus the trim coil setting used in (a).*

After correcting for optical distortion [13] and interpolating the measured thermal footprints from different infrared cameras onto a unified divertor grid [14], the heat flux can be calculated using the DLEVER code [6]. Fig. 7 presents three experimental results of the integrated power on the divertor: (a) the case with the largest Rstd ~ 0.85 ($I_{\mathrm{trim}} = -109$ A at $\varphi = -162^{\circ}$) from the trim coil phase scans, (b) the case with optimal b_{11} error field correction, and (c) the case with both optimal b_{11} and b_{22} error field corrections. The waveform in case (a) clearly exhibits a superposition of $cos\varphi$ and $cos2\varphi$, as described in Section 2.1.2, and can be fitted using the function $a_0 + a_1 cos\varphi + a_2 cos2\varphi$, with fitting parameters shown in the legend. After correcting b_{11}, the fitted amplitude a_1 is strongly reduced, resulting in a waveform dominated by $cos2\varphi$ component, as shown in (b). Finally, in case (c), with both b_{11} and b_{22} fields corrected, the integral power waveform is nearly flat, indicating a highly symmetric heat load deposition across the machine modules.

In addition, as a confirmation of our experimental results, in (d) the divertor heat loads are simulated using EMC3-Lite, with an inverted sign for the best trim and control coil settings (mimicking intrinsic error fields) plus the trim coil setting in case (a). The simulated results are qualitatively consistent with the experimental results in the trend of the waveforms, although the asymmetry level is rather reduced. Notice that we use the same input parameters for the simulation as stated in Section 2.1.2. Fine-tuning of these parameters may produce a better agreement with experiments but this is not the aim of the present study. Additional factors which may cause mismatches between experiments and simulations include: other uncorrected side bands of the intrinsic error fields, harmonics introduced by the trim and control coils (as shown in 2.1.1), finite divertor misalignments, and the reduced heat transport physics in EMC3-Lite.

It is noteworthy that the successful correction of both b_{11} and b_{22} error fields is largely attributable to the insights gained from previous studies [2,3]. This validates the experimentally determined optimal trim coil settings used in the 2017 campaign with divertor thermocouples, despite the use of inertially cooled test divertor units at that time and a slight variation in the standard magnetic configuration—specifically, planar coils increasing the rotational transform compared to the present study. These results suggest that both the magnetic coil systems and the intrinsic error fields have remained remarkably stable over approximately seven years. Furthermore, the findings provide good confirmation of the simulation predictions [2] for the phase and amplitude of the b_{22} error field, which were derived from fitting the flux surface mapping results following b_{11} error field correction in a narrow-mirror magnetic configuration with 5/5 boundary islands, similar to the standard configuration.

3. CONCLUSION

Divertor heat loads, calculated from the measured surface temperatures of all ten divertor units using infrared cameras, are employed to support a quantitative study of intrinsic error fields in W7-X. For the first time, in addition to the b_{11} error field correction using trim coils, the intrinsic b_{22} error field is corrected by symmetrizing the divertor integrated power through a phase scan experiment employing control coils. The experimental design was guided by comprehensive simulations, which established a direct link between coil current waveforms and the resulting perturbation fields. Furthermore, simulations of divertor heat loads under perturbation fields indicate that the typical heat load distribution can be represented as a superposition of cosine functions. With the b_{22} error field corrected, a significant improvement in the symmetry of heat loads is achieved—an enhancement that cannot be realized with trim coils alone. The experimental results also support previous findings [3] regarding the phase and amplitude of the b_{11} error field obtained during the first divertor campaign, suggesting that the magnetic coil systems have maintained reliable and rigid mechanical integrity over the past seven years. Additionally, the newly achieved b_{22} error field correction confirms the simulation predictions [2] from flux surface mapping results.

ACKNOWLEDGEMENTS

This work has been carried out within the framework of the EUROfusion Consortium, funded by the European Union via the Euratom Research and Training Programme (Grant Agreement No 101052200 — EUROfusion). Views and opinions expressed are however those of the author(s) only and do not necessarily reflect those of the European Union or the European Commission. Neither the European Union nor the European Commission can be held responsible for them.

REFERENCES

[1] GEIGER, J., et al, Physics in the magnetic configuration space of W7-X, Plasma Phys. Control. Fusion **57** (2015) 014004.

[2] BOZHENKOV, S., et al., Measurements and correction of the 1/1 error field in Wendelstein 7-X, Nucl. Fusion **59** (2019) 026004.

[3] LAZERSON, S., et al., Error fields in the Wendelstein 7-X stellarator, Plasma Phys. Control. Fusion **60** (2018) 124002.

[4] JAKUBOWSKI, M., et al., Infrared imaging systems for wall protection in the W7-X, Review of Scientific Instruments **89**, 10E116 (2018).

[5] FELLINGER, J., et al., Manufacturing, installation, commissioning and operation of endoscopes for monitoring water-cooled divertor in Wendelstein 7-X, Fusion Engineering and Design **203** (2024) 114413.

[6] THIEDE, S., et al., **Master's thesis** (2023), University of Greifswald.

[7] HERRMANN, A., et al., Limitations for divertor heat flux calculations of fast events in tokamaks, 28th EPS Conference on Contr. Fusion and Plasma Phys. **25A** (2001) 2109-2112.

[8] RUMMEL, T., et al., The Trim Coils for the Wendelstein 7-X Magnet System, IEEE Transactions on Applied Superconductivity, **22**, 3 (2012).

[9] FÜLLENBACH, F., et al., Commissioning of the Wendelstein 7-X in Vessel Control Coils, IEEE Transactions on Plasma Science, **48**, 7 (2020).

[10] OTTE, M., et al., Setup and initial results from the magnetic flux surface diagnostics at Wendelstein 7-X, Plasma Phys. Control. Fusion **58** (2016) 064003.

[11] BOZHENKOV, S., et al., Service oriented architecture for scientific analysis at W7-X. An example of a field line tracer, Fusion Engineering and Design **88** (2013) 2997–3006.

[12] FENG, Y., Review of magnetic islands from the divertor perspective and a simplified heat transport model for the island divertor, Plasma Phys. Control. Fusion **64** (2022) 125012.

[13] PISANO, F., et al., Tools for Image Analysis and First Wall Protection at W7-X, Fusion Science and Technology **76** (2020) 933–941.

[14] GAO, Y., et al., Methods for quantitative study of divertor heat loads on W7-X, Nucl. Fusion **59** (2019) 066007.